

Discrete diffraction transform for propagation, reconstruction, and design of wavefield distributions

Vladimir Katkovnik,* Jaakko Astola, and Karen Egiazarian

Signal Processing Institute, University of Technology of Tampere, P. O. Box 553, Tampere, Finland

*Corresponding author: katkov@cs.tut.fi.

Received 31 January 2008; revised 6 May 2008; accepted 6 May 2008;
posted 22 May 2008 (Doc. ID 92256); published 24 June 2008

A discrete diffraction transform (DDT) is a novel discrete wavefield propagation model that is aliasing free for a pixelwise invariant object distribution. For this class of distribution, the model is precise and has no typical discretization effects because it corresponds to accurate calculation of the diffraction integral. A spatial light modulator (SLM) is a good example of a system where a pixelwise invariant distribution appears. Frequency domain regularized inverse algorithms are developed for reconstruction of the object wavefield distribution from the distribution given in the sensor plane. The efficiency of developed frequency domain algorithms is demonstrated by simulation. © 2008 Optical Society of America
OCIS codes: 070.2025, 100.3010, 100.3190.

1. Introduction

Wavefield reconstruction from intensity and phase measurements is one of the basic problems in digital wavefield imaging and holography [1]. In a typical holography scenario one distinguishes input/object and output/sensor planes (see Fig. 1). The object plane is a source of light radiation/reflection propagating along the optical axis. The sensor plane is parallel to the object plane with a distance z between the planes. The problem is to reconstruct the wavefield in the input/object plane from data in the output/sensor plane. Some of the usual algorithms mimic the optical procedure when the hologram is illuminated with the reference wave. To calculate the diffraction field in digital versions of these type of methods, a recorded hologram is multiplied by a complex-valued distribution that models the reference wave. Three images can be obtained simultaneously in this method: real object in-focus, virtual object out-of-focus, and low frequency zero order term. Further processing is required to separate these images. The

advantage of the procedure is that a single record of the hologram is required [1].

Different types of the algorithms can be used if we assume that wavefield information is available at the sensor plane. The corresponding complex-valued (intensity-phase) measurements can be obtained using the phase-shifting techniques, where few phase-shifting holograms have been recorded [1,2].

A contribution of this paper concerns a few aspects of digital modeling for optical wavefield propagation, reconstruction, and design. The first is a novel discrete diffraction transform (DDT) model of the wavefield propagation presented in Section 3. The model is accurate for a pixelwise invariant object distribution, i.e., for a distribution that is piecewise constant in rectangular elements of pixel size of the digital sensor. This discrete modeling gives accurate and aliasing free results for any pixel size. Here we refer to the aliasing appearing as a result of discretization in the standard discrete approximations of the wavefield propagation integrals. This precise modeling of the wavefield propagation imitates an "ideal" physical experiment as it is presented by the integral propagation equations. This sort of accurate modeling is useful for reliable design and

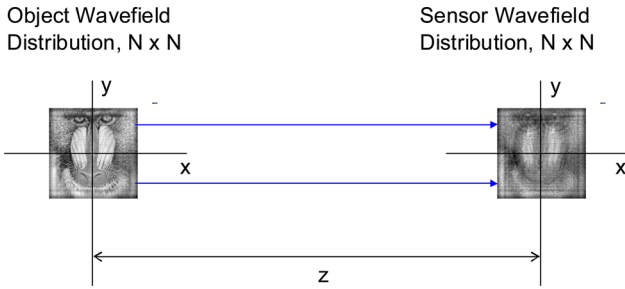


Fig. 1. (Color online) Principal setup of wavefield propagation and reconstruction.

computer testing of digital holography algorithms because the design and tests can be based on the precisely modeled observations. For an arbitrary continuous object distribution, the proposed wavefield propagation modeling is approximate with the accuracy depending on the accuracy of the piecewise fitting of the object wavefield distribution. A spatial light modulator (SLM) generating a pixelwise invariant wavefield distribution is a good example of the optical system where the developed digital modeling is relevant.

The DDT approach is different from the standard digital models usually used for holographic data. This approach is a signal/image processing view of the problem applied and developed for digital holography. The applications presented in this paper concern a wavefield reconstruction considered in two settings: object distribution reconstruction from a wavefield distribution given in the sensor plane (Section 4) and object distribution design with the goal of obtaining a desirable wavefield distribution at the sensor plane (Section 6). The developed frequency domain regularized inverse and recursive regularized inverse techniques show a very good performance in simulation experiments where the observed data are obtained according to the proposed accurate forward propagation modeling. The approach we present in this paper is based on the work we presented in [3].

2. Standard Models of Wavefield Propagation

Consider wavefield propagation modeling for the setting shown in Fig. 1. Let $u_z(x, y)$ be a complex-valued 2D wavefield defined in the sensor plane z of the 3D space (x, y, z) as a function of the lateral coordinates x and y . According to the scalar diffraction theory, there is a linear operator which links this wavefield with the object wavefield $u_0(x, y)$ at $z = 0$ as $u_z(x, y) = \mathcal{D}_z\{u_0(x, y)\}$, where \mathcal{D}_z stands for a diffraction operator with a distance parameter z . The thorough theory of this operator representation can be found in [4].

The diffraction operator can be given as a convolution

$$u_z(x, y) = \int_{-\infty}^{\infty} \int_{-\infty}^{\infty} g_z(x - \xi, y - \eta) u_0(\xi, \eta) d\xi d\eta, \quad (1)$$

where the kernel g_z is shift invariant and has a form of the first Rayleigh–Sommerfeld solution of the Maxwell–Helmholtz equation $\nabla^2 u + k^2 u = 0$. Here $k = 2\pi/\lambda$ is the wave number and λ is the wavelength. This kernel is as follows [5]:

$$g_z = z \frac{\exp(j2\pi r/\lambda)}{j\lambda r^2}, \quad r = \sqrt{x^2 + y^2 + z^2}. \quad (2)$$

It is shown in [4] that the operator \mathcal{D}_z is invertible, and this inverse operator also can be presented as a convolution with a shift-invariant kernel. If the diffraction wavefield $u_z(x, y)$ is given, then the wavefield at the input object plane $z = 0$ can be reconstructed using the inverse operator \mathcal{D}_z^{-1} , i.e., $u_0(x, y) = \mathcal{D}_z^{-1}\{u_z(x, y)\}$.

The term *diffraction transform* is used in [4] for these forward \mathcal{D}_z and backward \mathcal{D}_z^{-1} operators. Thus, the reconstruction problem is reduced to calculation of the inverse transform and the corresponding wavefield.

One of the fundamental results of the scalar diffraction theory (with two different proofs presented in [4,5]) is that the 2D integral Fourier transform of the kernel g_z has a form

$$G_z(f_x, f_y) = \mathcal{F}\{g_z(x, y)\} = \begin{cases} \exp(j2\pi \frac{z}{\lambda} \sqrt{1 - (\lambda f_x)^2 - (\lambda f_y)^2}), & (f_x, f_y) \in D_\lambda \\ 0, & \text{otherwise} \end{cases} \quad (3)$$

Here f_x and f_y are the Fourier transform frequencies and the disc $D_\lambda = \{(f_x, f_y) : (\lambda\omega_x)^2 + (\lambda\omega_y)^2 < 1\}$ defines the area where the transfer function G_z of the operator is nonzero.

In the frequency domain the forward and inverse diffraction transforms are given by

$$U_z(f_x, f_y) = G_z(f_x, f_y) U_0(f_x, f_y), \quad (4)$$

$$U_0(f_x, f_y) = G_z^*(f_x, f_y) U_z(f_x, f_y), \quad (5)$$

where $U_z(f_x, f_y) = \mathcal{F}\{u_z(x, y)\}$ and $G_z^*(f_x, f_y)$ is a complex conjugate of $G_z(f_x, f_y)$, $G_z^*(f_x, f_y) = G_{-z}(f_x, f_y)$. It proves that the inverse diffraction transform can be obtained from the forward one by replacing z with $-z$ in the kernel and in the transfer function.

Thus, the diffraction transform with the kernel g_z is a lowpass filter with the amplitude characteristic $|G_z(f_x, f_y)| = 1$ and with the phase $\psi_{G_z} = 2\pi(z/\lambda) \times [1 - (\lambda\omega_x)^2 - (\lambda\omega_y)^2]^{1/2}$ on the disc D_λ .

As $|G_z(f_x, f_y)| = 1$ the diffraction transform is not only invertible but well-conditioned on D_λ . This inverse does not require regularization typical for ill-conditioned inverse problems.

If the spectra $U_z(f_x, f_y)$ and $U_0(f_x, f_y)$ are given, the corresponding wavefields are calculated by the

inverse integral Fourier transform for $U_z(f_x, f_y)$ having the form

$$u_z(x, y) = \int \int U_z(f_x, f_y) \exp(-j2\pi(f_x x + f_y y)) df_x df_y. \quad (6)$$

Calculating the inverse Fourier transform from Eq. (5), we derive an analytical expression for the kernel of the inverse diffraction transform as g_{-z} , indeed

$$\begin{aligned} u_0(x, y) &= \mathcal{D}_z^{-1}\{u_z(x, y)\} \\ &= \int \int g_{-z}(x - \xi, y - \eta) u_z(\xi, \eta) d\xi d\eta \\ &= \mathcal{D}_{-z}\{u_z(x, y)\}. \end{aligned} \quad (7)$$

Discretization of the integral diffraction transforms defined by the formulas (1) and (6) is a natural idea to derive the digital models for the forward and backward wavefield propagation. It is well known that this discretization is far from being trivial.

The principal difficulty of discretization in the space domain (1) follows from the fact that the kernel g_z is modulated by a strongly fluctuated high-frequency harmonic factor $\exp(j2\pi r/\lambda)$. The discrete sampling of the rate at least twice higher than the highest frequency component of the integrand is a standard remedy. Obviously it can result in an unacceptably high sampling rate.

The integration in the frequency domain in Eq. (6) appears to be an attractive alternative because, for $|f_x| \ll 1/\lambda$ and $|f_y| \ll 1/\lambda$, the phase $\psi_{G_z} \simeq 2\pi \frac{z}{\lambda} - \pi z \lambda (f_x + f_y)$ is slowly varying in f_x and f_y . However, formula (3) is derived assuming that the sensor domain is infinite in the lateral coordinates. A finite (usually small size) sensor means that the infinitely extended sensor plane is multiplied by the 2D rectangular window function, which has a magnitude of one for the sensor area and zero elsewhere. In the frequency domain this multiplication causes the convolution of the spectrum $U_z(f_x, f_y)$ in Eq. (6) with the 2D sinc function.

The discrete modeling of the diffraction transform is a subject of many publications. The review of this area is beyond the scope of this paper. However, we wish to mention that the discrete space domain modeling for holography is discussed in detail in [1], and the accuracy of the frequency domain approach is analyzed in [6]. The fast Fourier transform (FFT) based algorithm with a detailed accuracy analysis is presented in [7]. The stationary phase method applied for integration in Eq. (6) results in discrete models with a nonuniform sampling in the frequency domain (e.g., [8]). A number of recent developments concern continuous and discrete Fresnel transforms and their multiresolution versions (e.g., [9–11]).

One of the simple standard convolution-based discrete models is obtained from the continuous domain

Fourier representations (4) and (5). For square object and sensor arrays of $N \times N$ pixels with pixel size $\Delta \times \Delta$ this discrete model follows from Eqs. (4) and (5), where FFT is used instead of the integral Fourier transform (e.g., [1,2]):

$$\bar{U}_z(v_x, v_y) = \bar{G}_z(v_x, v_y) \bar{U}_0(v_x, v_y), \quad (8)$$

$$\bar{U}_0(v_x, v_y) = \bar{G}_z^*(v_x, v_y) \bar{U}_z(v_x, v_y). \quad (9)$$

where $\bar{U}_z = \mathcal{FFT}\{u_z\}$, $\bar{U}_0 = \mathcal{FFT}\{u_0\}$, and $\bar{G}_z = \mathcal{FFT}\{g_z\}$ are calculated over the $N \times N$ arrays, and v_x and v_y are the FFT frequencies.

3. Discrete Diffraction Transform

The standard techniques, particularly those mentioned above, consider the discrete models as approximation for underlying continuous ones given in continuous variables and in integral forms. The sampling and aliasing issues are of importance for these approximations as they define preconditions for reconstruction of continuous signals from sampled ones.

The motivation for the discrete model developed in this paper is different. Let us assume that the input distribution is discrete, defined by a pixelwise constant object wavefield distribution, and the output is also discrete, as defined by the outputs of the sensor pixels. For this pixelwise constant modeling, we accurately calculate the propagation (1). Thus, we arrive at discrete-to-discrete modeling, where the inputs are pixel values of the object distribution and the outputs are the pixel values of the digital sensor output. This model is precise as the accurate integration of propagation (1) is assumed.

In this development the standard assumptions concerning the sampling and band limitedness can be omitted as they are replaced by the hypothesis that the object plane distribution is piecewise constant or well approximated by this sort of distribution. A relevant interesting discussion on similar issues of signal modeling for wavefield propagation can be seen in [9].

We named the proposed discrete propagation model a discrete diffraction transform (DDT). It is represented in space and frequency domains. We give the corresponding formulas assuming that the object and sensor arrays are of $N_0 \times N_0$ and $N_z \times N_z$ pixels, respectively, and the pixels are square with equal dimensions $\Delta \times \Delta$.

A. Space Domain DDT

Let us derive the formulas for DDT. Assume that the distribution u_0 allows a pixelwise constant approximation, i.e., the distribution is piecewise invariant in rectangular elements of pixel size of the digital sensor. Then the integral (1) can be represented as

$$\begin{aligned}
u_z(x, y) &= \sum_{s, t = -N_0/2}^{N_0/2-1} u_0[s, t] \int_{-\Delta/2}^{\Delta/2} \int_{-\Delta/2}^{\Delta/2} g_z(x - s\Delta + \xi, y \\
&\quad - t\Delta + \eta) d\xi d\eta, \\
u_0[s, t] &= u_0(s\Delta + \xi, t\Delta + \eta), -\Delta/2 \leq \xi, \eta < \Delta/2,
\end{aligned} \tag{10}$$

where the sum is calculated over the square array of $N_0 \times N_0$ pixels.

Let the output signal of a sensor's pixel be the mean value of the distribution impinging on this pixel:

$$u_z[k, l] = \frac{1}{\Delta^2} \int_{-\Delta/2}^{\Delta/2} \int_{-\Delta/2}^{\Delta/2} u_z(k\Delta + \xi', l\Delta + \eta') d\xi' d\eta'. \tag{11}$$

Inserting Eq. (10) into Eq. (11), we arrive at the space domain DDT, given as a discrete convolution

$$\begin{aligned}
u_z[k, l] &= \sum_{s, t = -N_0/2}^{N_0/2-1} a_z[k - s, l - t] u_0[s, t], \\
k, l &= -N_z/2 + 1, \dots, N_z/2 - 1,
\end{aligned} \tag{12}$$

where the kernel is calculated as

$$\begin{aligned}
a_z[k, l] &= \frac{1}{\Delta^2} \int_{-\Delta/2}^{\Delta/2} \int_{-\Delta/2}^{\Delta/2} \int_{-\Delta/2}^{\Delta/2} \int_{-\Delta/2}^{\Delta/2} g_z(k\Delta + \xi' \\
&\quad + \xi, l\Delta + \eta' + \eta) d\xi d\eta d\xi' d\eta', \\
k, l &= -N_a/2 + 1, \dots, N_a/2 - 1, N_a = N_0 + N_z.
\end{aligned} \tag{13}$$

The kernel a_z in Eq. (12) is a smoothed (double-smoothed) version of the original kernel g_z in Eq. (1). The smoothing in Eq. (11) takes into consideration discretization for both the object and sensor arrays.

It is obvious that, for a pixelwise constant object distribution u_0 , the models (12) and (13) are accurate, i.e., it gives the precise distribution for the sensor plane. Note that this statement is valid provided that the pixel grids in the object and sensor planes are identical and perfectly aligned.

For small Δ , such that $\Delta/z \rightarrow 0$ and $\Delta/\lambda \rightarrow 0$,

$$a_z[k, l] \xrightarrow{\Delta \rightarrow 0} \Delta^2 g_z(k\Delta, l\Delta). \tag{14}$$

This means that the kernel smoothing effect becomes negligible for small Δ , and a_z can be calculated using the simple formula (14), instead of Eq. (13), where g_z is given in Eq. (2).

The space domain model (12) can be rewritten in the vector-matrix form

$$\mathbf{u}_z = \mathcal{A}_z \cdot \mathbf{u}_0, \tag{15}$$

where $\mathbf{u}_z \in R^{N_z^2}$ and $\mathbf{u}_0 \in R^{N_0^2}$ are vectors formed from $u_z[k, l]$ and $u_0[k, l]$, respectively, and the \mathcal{A}_z matrix $N_z^2 \times N_0^2$ is formed from $a_z[k, l]$. If \mathcal{A}_z is a full rank matrix and $N_z \geq N_0$, a perfect reconstruction of \mathbf{u}_0 from \mathbf{u}_z is possible in the following form:

$$\mathbf{u}_0 = (\mathcal{A}_z^H \mathcal{A}_z)^{-1} \mathcal{A}_z^H \mathbf{u}_z, \tag{16}$$

where \mathcal{A}_z^H is a Hermitian conjugate of \mathcal{A}_z .

However, for usual sensor sizes (say 512×512 or 1024×1024 pixels) the dimension of the space domain model (12) becomes too high for practical calculations for both the forward prediction of \mathbf{u}_z from \mathbf{u}_0 and the backward inverse with reconstruction of \mathbf{u}_0 from \mathbf{u}_z . Note that the matrix \mathcal{A}_z is nonsparse, and the sparsity cannot be applied for more efficient calculations.

B. Frequency Domain DDT

FFT cannot be used directly for calculation of the convolution (12) even when $N_0 = N_z = N$ because, in this case, while the input u_0 and output u_z have the same size $N \times N$, the support size of the kernel a_z is much larger: $(2N - 1) \times (2N - 1)$.

To make FFT applicable we use zero-padding of the variables u_0 and u_z , extended to the extended size $N_a \times N_a$ and $N_a = N_0 + N_z$, covering the support of the kernel a_z . In what follows the wave tilde ($\tilde{}$) means that the corresponding variables extend by zero-padding to the size $N_a \times N_a$. The proposed frequency domain algorithm works with these extended size variables and exploits the advantage of FFT for fast and accurate calculation of the convolution (12).

The frequency domain calculation of DDT is produced according the following four step algorithm:

- Define FFT for u_0 extended to the size $N_a \times N_a$:

$$\begin{aligned}
\tilde{U}_0(v_x, v_y) &= \mathcal{FFT}\{\tilde{u}_0\} = \sum_{k, l = -N_0/2}^{N_0/2-1} u_0[k, l] W^{v_x k} W^{v_y l} \\
&= \sum_{k, l = -N_a/2}^{N_a/2-1} \tilde{u}_0[k, l] W^{v_x k} W^{v_y l}, \\
W &= \exp(-j2\pi/(2N)), \\
v_x, v_y &= -N_a/2, \dots, N_a/2 - 1.
\end{aligned} \tag{17}$$

- Take FFT of the DDT kernel to obtain the DDT transfer function:

$$\begin{aligned}
\tilde{A}_z(v_x, v_y) &= \mathcal{FFT}\{\tilde{a}_z\} = \sum_{u, v = -N_a/2+1}^{N_a/2-1} a_z[u, v] W^{v_x u} W^{v_y v} \\
&= \sum_{u, v = -N_a/2}^{N_a/2-1} \tilde{a}_z[u, v] W^{v_x u} W^{v_y v}.
\end{aligned} \tag{18}$$

- Calculate FFT for u_z extended to the size $N_a \times N_a$:

$$\begin{aligned}\tilde{U}_z(v_x, v_y) &= \tilde{A}_z(v_x, v_y) \tilde{U}_0(v_x, v_y), \\ \tilde{u}_z[k, l] &= \mathcal{FFT}^{-1}\{\tilde{U}_z(v_x, v_y)\}, \\ k, l &= -N_a/2, \dots, N_a/2 - 1.\end{aligned}\quad (19)$$

- Calculate u_z of the original size $N_z \times N_z$:

$$u_z[k, l] = \tilde{u}_z[k, l], \quad k, l = -N_z/2, \dots, N_z/2 - 1. \quad (20)$$

The following proposition states that the space domain formula (12) and the frequency domain algorithm (17)–(20) give identical results.

Proposition 1. Formulas (12) and (20) give identical $u_z[k, l]$, $k, l = -N_z/2, \dots, N_z/2 - 1$, for any $u_0[s, t]$, $s, t = -N_0/2, \dots, N_0/2 - 1$, and any even N_z and N_0 .

The proof is given in Appendix A.

Note that both the space and frequency domain DDT models are symmetrized with respect to the optical axis.

The frequency domain DDT is essentially different from its frequency integral counterpart (6) in two important aspects. DDT accurately takes into consideration a finite size of the sensor and, as a result, the DDT operator in general is ill-conditioned while the module of the transfer function $U_z(f_x, f_y)$ in Eq. (6) is equal to one and the corresponding operator is well-conditioned. In the frequency domain the conditioning of the DDT is measured as the ratio of the maximal-to-minimal value of the module of the transfer function [12],

$$\text{cond}_{\tilde{A}} = \max_{v_x, v_y} |\tilde{A}_z(v_x, v_y)| / \min_{v_x, v_y} |\tilde{A}_z(v_x, v_y)|. \quad (21)$$

Let the sensor and object planes have a size of $0.01 \text{ m} \times 0.01 \text{ m}$ and a wavelength of $\lambda = 0.632 \text{ nm}$. Figure 2 shows the dependence of the conditioning number $\text{cond}_{\tilde{A}}$ with respect to the distance z for $N_0 = N_z = 512$ ($\Delta = 0.01/512 \text{ m}$) and $N_0 = N_z = 1024$ ($\Delta = 0.01/1024 \text{ m}$). The conditioning number is approximately the linear growing function of z . The larger N and smaller Δ result in larger conditioning numbers. For distance z approximately equal to 1, the conditioning numbers are of the order 10^4 .

The amplitude and phase frequency characteristics of the transfer functions $\tilde{A}_z(v_x, v_y)$ for $\Delta = 0.01/1024 \text{ m}$ and small $\Delta \rightarrow 0$, $z = 0.75 \text{ m}$ is demonstrated in Figs. 3 and 4, respectively. The images are centered with respect to the zero-frequency $v_x = v_y = 0$.

These amplitude characteristics are typical for lowpass filters. The amplitude characteristic of $\tilde{A}_z(v_x, v_y)$ with $\Delta = 0.01/1024 \text{ m}$ is visually smoother than that for small $\Delta \rightarrow 0$ when the smoothing effects of averaging over the pixel surface disappear. The corresponding phase characteristics are very

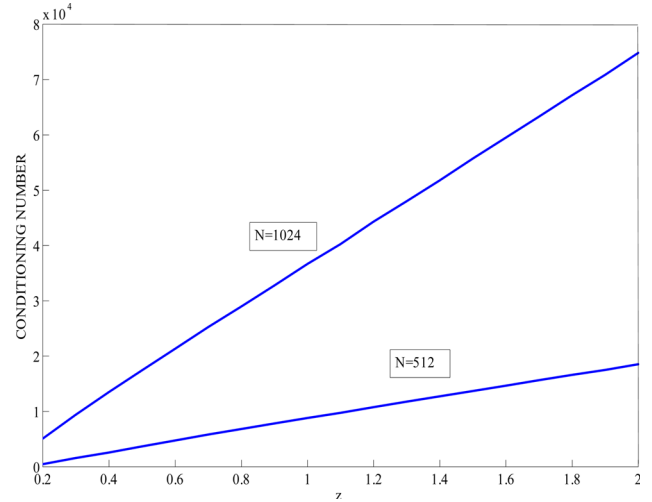


Fig. 2. (Color online) Conditioning number versus the distance z for the transfer function \tilde{A}_z with $N = 512$, $N = 1024$ and $\lambda = 0.632 \text{ nm}$.

different even though their images are similar in structure.

C. Fresnel Approximation

If $z \gg x$ and $z \gg y$ the following Fresnel approximation of the kernel g_z is valid,

$$g_z \simeq \frac{1}{j\lambda z} \exp \left[j \left(\frac{2\pi z}{\lambda} + \frac{\pi}{\lambda z} (x^2 + y^2) \right) \right]. \quad (22)$$

Then formula (13) can be simplified and allows the following factorization:

$$\alpha_z[k, l] \simeq \frac{\exp(j2\pi z/\lambda)}{j\lambda z} \rho_{z,\lambda}[k] \rho_{z,\lambda}[l], \quad (23)$$

where

$$\begin{aligned}\rho_{z,\lambda}[k] &= \frac{1}{\Delta} \int_{-\Delta/2}^{\Delta/2} \int_{-\Delta/2}^{\Delta/2} \exp \left(j \frac{\pi}{\lambda z} (k\Delta + \xi' + \xi)^2 \right) d\xi d\xi' \\ &= \Delta \int_{-1/2}^{1/2} \int_{-1/2}^{1/2} \exp \left(j \frac{\pi}{\lambda z} (k\Delta + \xi'\Delta + \xi\Delta)^2 \right) d\xi d\xi' \\ &= 2\Delta \int_{-1}^1 (1 - |v|) \exp \left(j \frac{\pi}{\lambda z} (k\Delta + \Delta v)^2 \right) dv.\end{aligned}\quad (24)$$

The proof that the double integral in Eq. (24) can be calculated as a single variable integral is given in Appendix B. For the Fresnel approximation the transfer function (18) is of the form

$$\tilde{A}_z(v_x, v_y) = \frac{\exp(j2\pi z/\lambda)}{j\lambda z} \Lambda_{z,\lambda}(v_x, N_a) \times \Lambda_{z,\lambda}(v_y, N_a), \quad (25)$$

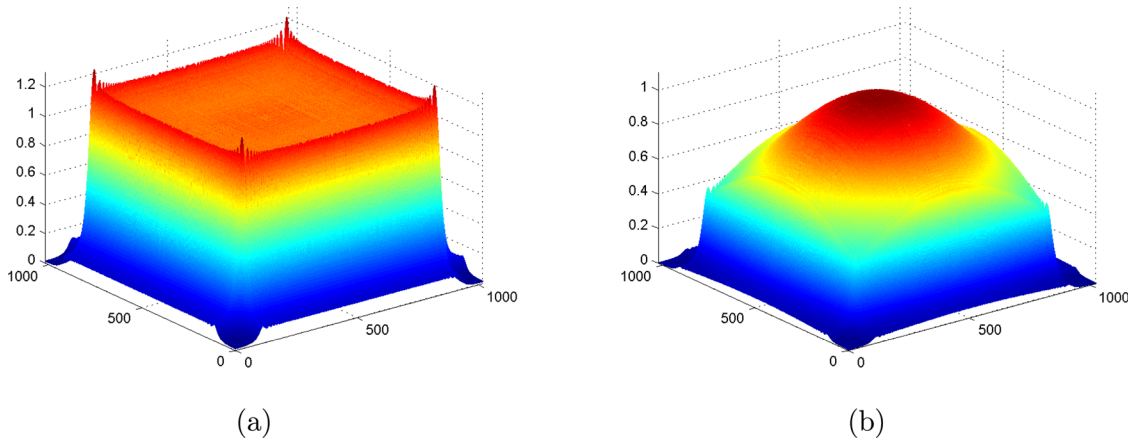


Fig. 3. (Color online) Module frequency characteristics of the discrete diffraction transfer function: (a) $\Delta \rightarrow 0$; (b) $\Delta = 0.01/1024$, $z = 0.75$ m.

where

$$\Lambda_{z,\lambda}(v, N) = \sum_{k,l=-N/2}^{N/2-1} \rho_{z,\lambda}[k] W^{vk},$$

$$W = \exp(-j2\pi/N_a),$$

$$v = -N_a/2, \dots, N_a/2 - 1. \quad (26)$$

The kernel a_z (13) and the transfer function \tilde{A}_z (18) are defined by the general wavefield propagation model. The Fresnel approximation allows significantly simplified calculations because the kernel $a_z[k, l]$ in Eq. (23) is calculated through the product of 1D $\rho_{z,\lambda}[k]$ and $\rho_{z,\lambda}[l]$. In a similar way, the 2D transfer function $\tilde{A}_z(v_x, v_y)$ in Eq. (25) is factorized in the product of $\Lambda_{z,\lambda}(v_x, N_a)$ and $\Lambda_{z,\lambda}(v_y, N_a)$.

For any wavelength λ and z the integration in Eq. (24) can be produced numerically with any desirable accuracy. Note that for the considered linear model the kernel a_z does not depend on the input

signal, thus it can be calculated only once for the given parameters and can be used for any input signals.

It is useful to note that, for small Δ/z and Δ/λ , we do not need to calculate the integrals (13) and (24) because $\rho_{z,\lambda}[k] \rightarrow \Delta \exp[j(\pi/\lambda z)(k\Delta)^2]$. In this case, the frequency domain algorithm (17)–(20) is similar to the integration FFT algorithm proposed in [7] for the squared input/output arrays u_0 and u_z , where these arrays are zero padded to the size $(N_a - 1) \times (N_a - 1)$ and $N_a = 2N_0$. It is done in order to obtain the circular convolution and the transfer function \tilde{A}_z calculated as FFT of the kernel g_z , defined on the extended grid $(N_a - 1) \times (N_a - 1)$.

4. Wavefield Reconstruction

It is well known that a reconstruction of the object wavefield u_0 from u_z is an inverse problem. Let us begin with a discussion of specific features of this problem as a result of the extended-size variables

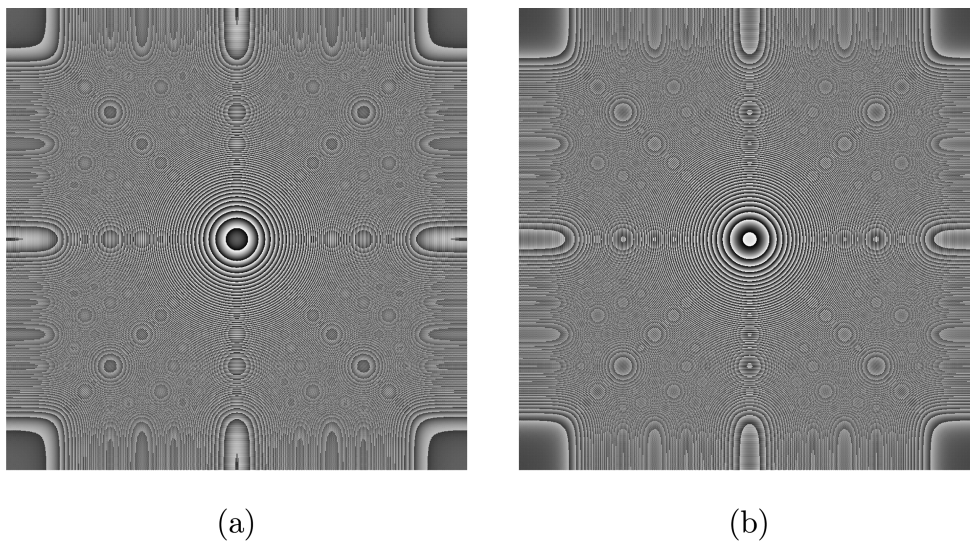


Fig. 4. Phase frequency characteristics of the discrete diffraction transfer function: (a) $\Delta \rightarrow 0$; (b) $\Delta = 0.01/1024$, $z = 0.75$ m.

that make the problem essentially different from standard settings.

A. Reconstruction as a Boundary Inverse Problem

It is convenient to consider this inverse reconstruction with both the space and frequency domains in parallel. Using the representation similar to Eq. (15), the extended size inverse problem can be formulated in the algebraic form as

$$\tilde{\mathbf{u}}_z = \tilde{\mathcal{A}}_z \cdot \tilde{\mathbf{u}}_0, \quad (27)$$

where $\tilde{\mathbf{u}}_z, \tilde{\mathbf{u}}_0 \in R^{N_a^2}$, and $\tilde{\mathcal{A}}_z = \begin{pmatrix} \mathcal{A}_z^{11} & \mathcal{A}_z^{12} \\ \mathcal{A}_z^{21} & \mathcal{A}_z^{22} \end{pmatrix}$ is a structured $N_a^2 \times N_a^2$ matrix. All submatrices in $\tilde{\mathcal{A}}_z$ are formed from $\tilde{a}_z[k, l]$.

The conditions when system (27) has a unique solution for $\tilde{\mathbf{u}}_0$ are formulated in the following proposition.

Proposition 2. Let $N_z \geq N_0$ and

$$\Lambda_{z,\lambda}(f, N_a) \neq 0, \quad \forall f = -N_a/2, \dots, N_a/2 - 1, \quad (28)$$

then system (27) has a unique solution.

The proof of the proposition is given in Appendix C.

The conditions (28) are necessary and sufficient for nonsingularity of the extended size DDT operator. It is difficult to prove that the discrete function $\Lambda_{z,\lambda}(f, N_a)$ never takes zero value. However, these conditions can be easily checked numerically for the finite set of frequencies f in (28). In our experiments with a variety of λ, Δ , and N_a we never met a situation when $\Lambda_{z,\lambda}(f, N_a)$ took a zero value for f from the interval $[-N_a/2, \dots, N_a/2 - 1]$. Thus, practically, system (27) always has a unique solution. This statement implies that, for any given $\tilde{\mathbf{u}}_z$, the corresponding unique $\tilde{\mathbf{u}}_0$ can always be found. The reconstruction of \mathbf{u}_0 from Eq. (27) requires further detailing.

Let the vectors $\tilde{\mathbf{u}}_z$ and $\tilde{\mathbf{u}}_0$ in Eq. (27) be structured as follows: $\tilde{\mathbf{u}}_z = (u'_z \ u_z)$ and $\tilde{\mathbf{u}}_0 = (\mathbf{u}_0 \ \mathbf{u}'_0)$, where \mathbf{u}_z and \mathbf{u}_0 are the main variables from Eq. (15), and $\mathbf{u}'_z \in R^{N_a^2 - N_z^2}$ and $\mathbf{u}'_0 \in R^{N_a^2 - N_0^2}$ are the vectors of the idle variables complementing the vectors $\tilde{\mathbf{u}}_z$ and $\tilde{\mathbf{u}}_0$ to the extended size. It is obvious that, for these structured vectors, $\mathcal{A}_z^{11} = \mathcal{A}$ from Eq. (15). It follows from Eq. (20) that $\mathbf{u}'_0 = 0$.

In the inverse problem of our interest the vector, $\mathbf{u}_z = \mathbf{u}_z^\#$ is given, and the vectors \mathbf{u}_0 and \mathbf{u}'_z are unknown. Thus we arrive at the equation

$$\begin{pmatrix} \mathbf{u}_z^\# \\ \mathbf{u}'_z \end{pmatrix} = \tilde{\mathcal{A}}_z \begin{pmatrix} \mathbf{u}_0 \\ \mathbf{0} \end{pmatrix}, \quad (29)$$

with a total number of the equations N_a^2 and N_0^2 unknowns as the items of the vector \mathbf{u}_0 and $(N_a^2 - N_0^2)$ unknowns as the items of the vector \mathbf{u}'_z . Thus, there is the accurate balance of the number of the unknowns and the equations at hand.

The solution of Eq. (29) is a boundary problem as the unknown \mathbf{u}'_z is in the left side of the equation and

the unknown \mathbf{u}_0 is in the right side of the equation. Equation (29) is resolved with respect to \mathbf{u}'_z . We can invert $\tilde{\mathcal{A}}_z$ to resolve this equation with respect to \mathbf{u}_0

$$\begin{pmatrix} \mathbf{u}_0 \\ \mathbf{0} \end{pmatrix} = \tilde{\mathcal{A}}_z^{-1} \begin{pmatrix} \mathbf{u}_z^\# \\ \mathbf{u}'_z \end{pmatrix}. \quad (30)$$

The boundary inverse problem can be solved iteratively using Eqs. (29) and (30) and starting from the initialization of $\mathbf{u}_z^{(0)} = 0$:

$$\begin{pmatrix} \hat{\mathbf{u}}_0^{(r)} \\ \hat{\mathbf{u}}_z^{(r)} \end{pmatrix} = \tilde{\mathcal{A}}_z^{-1} \begin{pmatrix} \mathbf{u}_z^\# \\ \hat{\mathbf{u}}_z^{(r-1)} \end{pmatrix}, \quad (31)$$

$$\begin{pmatrix} \hat{\mathbf{u}}_z^{(r)} \\ \hat{\mathbf{u}}_0^{(r)} \end{pmatrix} = \tilde{\mathcal{A}}_z \begin{pmatrix} \hat{\mathbf{u}}_0^{(r)} \\ \mathbf{0} \end{pmatrix}, \quad r = 1, \dots \quad (32)$$

Here $\mathbf{u}_0^{(r)}$ and $\hat{\mathbf{u}}_z^{(r)}$ are the idle variables, while $\hat{\mathbf{u}}_0^{(r)}$ is a variable of the interest. In what follows we use the FFT domain version of Eqs. (31) and (32) to obtain the fast and efficient implementation of the recursive procedure (31) and (32), where the inverse $\tilde{\mathcal{A}}_z^{-1}$ is replaced by the regularized inverse because $\tilde{\mathcal{A}}_z$ is ill-conditioned.

B. Regularized Inverse

Let us start from a simple algorithm for the inverse. Assume that $\tilde{U}_z(v_x, v_y)$ in Eq. (19) is known as given by the observations and introduces the following quadratic criterion defining the accuracy fit of the model $\tilde{\mathcal{A}}_z \tilde{U}_0$ to the given \tilde{U}_z :

$$J = \|\tilde{U}_z - \tilde{\mathcal{A}}_z \tilde{U}_0\|^2 + \alpha \|\tilde{U}_0\|^2. \quad (33)$$

Here $\|\cdot\|^2$ is the Euclidean norm calculated over the FFT frequencies v_x and v_y ; and $\|\tilde{U}_0\|^2$ and $\alpha > 0$ are a regularization penalty term and a regularization parameter, respectively. This regularization is of special importance when the DDT is ill-conditioned and/or the observations \tilde{U}_z are noisy [13,12,14].

Minimization of J with respect to \tilde{U}_0 gives the minimum condition in the form $\partial J / \partial \tilde{U}_0^* = 0$ and the following solution (e.g., [14])

$$\hat{U}_0 = \tilde{\mathcal{A}}_z^* \cdot \tilde{U}_z / (|\tilde{\mathcal{A}}_z|^2 + \alpha^2). \quad (34)$$

Finally we obtain

$$\begin{aligned} \hat{u}_0 &= \mathcal{F}FT^{-1}\{\hat{U}_0\}, & \hat{u}_0[k, l] &= \tilde{u}_0[k, l], \\ k, l &= -N_0/2, \dots, N_0/2 - 1. \end{aligned} \quad (35)$$

Here \hat{u}_0 is a regularized inverse estimate of the object wavefield distribution. The regularization parameter $\alpha > 0$ controls a level of smoothing in this estimate [12–14].

The frequency domain calculations in Eq. (34) are produced for the extended size $N_a \times N_a$ of u_0 and u_z . The zero-padding of the observations u_z usually

results in some ringing effects along the bounds of the reconstructed object distribution. An improved version of Eqs. (34) and (35), what we call a recursive regularized inverse, overcomes these effects, or at least diminishes them significantly.

C. Recursive Regularized Inverse

We propose the following recursive procedure defining the frequency domain and regularized version of the procedure (31) and (32). This algorithm is composed from backward (inverse) and forward transformations performed recursively for $r = 1, 2, \dots$:

a. For the backward propagation of (31), we produce the following successive calculations:

$$\begin{aligned} \tilde{u}_z^{(r-1)}[k, l] &= u_z^\# [k, l], \quad k, l = -N_z/2, \dots, N_z/2 - 1, \\ \tilde{U}_z^{(r)}[v_x, v_y] &= \mathcal{F}\mathcal{F}\mathcal{T}\{\tilde{u}_z^{(r-1)}[k, l]\}, \\ \tilde{U}_0^{(r)}[v_x, v_y] &= \tilde{A}_z^*/(|\tilde{A}_z|^2 + \alpha^2) \cdot \tilde{U}_z^{(r)}[v_x, v_y]; \end{aligned} \quad (36)$$

$$\tilde{u}_0^{(r)}[s, t] = \mathcal{F}\mathcal{F}\mathcal{T}^{-1}\{\tilde{U}_0^{(r)}[v_x, v_y]\}; \quad (37)$$

$$\tilde{u}_0^{(r)}[s, t] = 0, \quad \text{for all } s, t \notin [-N_0/2, \dots, N_0/2 - 1]. \quad (38)$$

b. For the forward propagation of (32), we produce the following successive calculations:

$$\begin{aligned} \tilde{U}_0^{(r)}[v_x, v_y] &= \mathcal{F}\mathcal{F}\mathcal{T}\{\tilde{u}_0^{(r)}[s, t]\}, \\ \tilde{U}_z^{(r)}[v_x, v_y] &= \tilde{A}_z[v_x, v_y]\tilde{U}_0^{(r)}[v_x, v_y], \\ \tilde{u}_z^{(r-1)}[k, l] &= \mathcal{F}\mathcal{F}\mathcal{T}^{-1}\{\tilde{U}_z^{(r-1)}[v_x, v_y]\}. \end{aligned} \quad (39)$$

c. Finally, the estimate of the object distribution u_0 follows from Eq. (38):

$$\hat{u}_0^{(r)}[s, t] = \tilde{u}_0^{(r)}[s, t], \quad s, t = -N_0/2, \dots, N_0/2 - 1. \quad (40)$$

The procedure of Eqs. (36)–(39) is initiated by $\tilde{u}_z^{(0)} = 0$.

The estimates $\hat{u}_0^{(r)}$ of Eq. (40) are obtained from the backward equations, while the forward equations are used for predictions $\tilde{u}_z^{(r-1)}$ of the observed data from the obtained estimate. The multiple experiments show that the algorithm (36)–(40) is quite efficient and provides a significant improvement of the regularized inverse estimate (34) and (35), which is the first step of this recursive algorithm.

The algorithm (36)–(40) easily incorporates *a priori* information on the object distribution. If the object is an amplitude modulator with the phase of

the object distribution equal to zero, then Eq. (37) is replaced by

$$\tilde{u}_0^{(r)}[s, t] = |\mathcal{F}\mathcal{F}\mathcal{T}^{-1}\{\tilde{U}_0^{(r)}[v_x, v_y]\}|. \quad (41)$$

If the object is a phase modulator of the amplitude equal to 1 then Eq. (37) is replaced by

$$\tilde{u}_0^{(r)}[s, t] = \exp[-j \times \text{angle}(\mathcal{F}\mathcal{F}\mathcal{T}^{-1}\{\tilde{U}_0^{(r)}[v_x, v_y]\})]. \quad (42)$$

This specification of the estimated object distribution improves the convergence and the accuracy of the algorithm.

5. Simulation Experiments for Wavefield Reconstruction

Let us illustrate the performance of the proposed inverse algorithm for different applications. In these numerical experiments we use the Baboon intensity distribution (512×512 pixels) imaged in Fig. 5. This distribution, denoted in what follows as $u^\#$, is real-valued nonnegative, $0 \leq u^\# \leq 1$. The parameters of the experiment are $\lambda = 0.632$ nm, $z = 0.5$ m, and $N_0 = N_z = N = 512$; the square sensor and object have the same size 0.01 m \times 0.01 m with the pixel size parameter $\Delta = 0.01/N$ m.

A. Sampling Conditions

The frequency of the varying on x harmonic factor $\exp[j\frac{\pi}{\lambda z}(x^2 + y^2)]$ of the kernel (2) is calculated as $2\pi x/\lambda z$. The maximum values of x are equal to half of the sensor linear size, $x_{\max} = 0.01/2 = 0.005$. Then the upper bound for the frequency is equal to $2\pi x_{\max}/\lambda z$. The Nyquist requirement for the non-aliasing sampling follows from the inequality $2\pi x_{\max}/\lambda z < \pi/\Delta$, i.e., $\Delta < \Delta_{\text{crit}} = \lambda z/2x_{\max}$. For the given sensor size, $\Delta_{\text{crit}} = 3.16 \times 10^{-5}$. It follows that for the selected parameters of the experiments

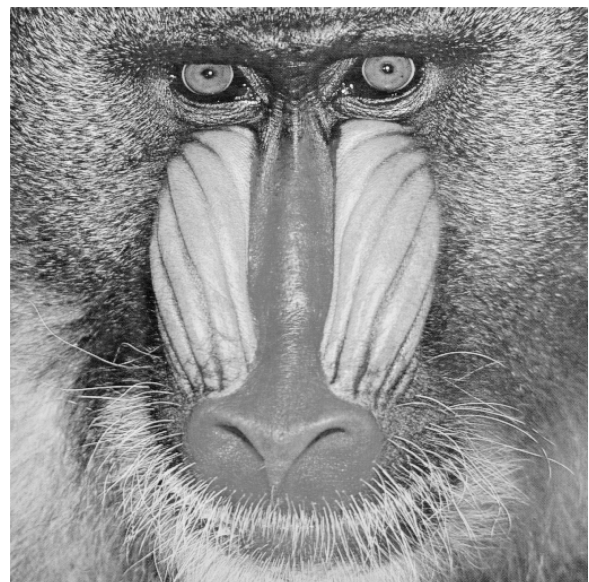


Fig. 5. Image of the Baboon test-distribution.

$\Delta = 0.01/512 = 1.95 \times 10^{-5} < \Delta_{\text{crit}}$, i.e., the Nyquist condition holds.

To demonstrate that DDT results in the aliasing free reconstructions, we begin with a case when the Nyquist condition is violated. Let Δ have a double size, $\Delta = 2 \times 1.95 \times 10^{-5} > \Delta_{\text{crit}}$. Assume that the true object distribution is real-valued $u_0 = u^\#$.

Figure 6 shows the amplitude and phase wavefield distributions at the sensor plane calculated according to the forward propagation model (17)–(20). It is emphasized once more that DDT gives the precise sensor plane distribution corresponding to the accurately calculated integral (1).

The object plane reconstructions are shown in Fig. 7. Figures 7(a) and 7(b) show the amplitude distributions in the object plane obtained by the DDT regularized inverse (34) and (35) and by the standard FFT (8) and (9) algorithm, respectively. The periodical pattern typical for the aliasing effects destroys the standard reconstruction shown in Fig. 7(b) completely, while the DDT-based algorithm demonstrates in Fig. 7(a) the quite accurate reconstruction of the Baboon test-distribution. This result confirms the ability of the DDT algorithm to perform well even when the Nyquist condition is violated.

In all forthcoming experiments we assume that $\Delta = 1.95 \times 10^{-5} < \Delta_{\text{crit}}$, i.e., the Nyquist condition holds. Then the standard FFT works but, qualitatively and numerically, the DDT technique enables better results. For quantitative numerical characterization of the accuracy of the reconstruction we use the root-mean-squared error (RMSE).

B. Amplitude Modulation

Let the true wavefield distribution in the object plane be real-valued $u_0 = u^\#$. The results obtained by the standard FFT and DDT algorithms can be seen in Fig. 8. Here, for the DDT reconstruction

we use the recursive regularized DDT algorithm (36)–(40). The results are given for the tenth iteration of this algorithm. Comparison of Fig. 8(a) versus Fig. 8(b) is in the favor of the recursive regularized DDT algorithm. It demonstrates a better visual quality as well as a lower RMSE value.

The regularized inverse estimate in Fig. 7(a) is a first iteration of the recursive regularized inverse algorithm. The ringing bands parallel to the boundaries in Fig. 7(a) are typical for the regularized inverse deconvolution algorithms. Comparing this image with that given in Fig. 8(a) we can note that the recursive regularized inverse allows to get rid of these disturbing effects and yields about twice better RMSE value.

C. Phase Modulation

Consider a reconstruction of the object phase distribution assuming that the true object distribution has a module equal to one and the phase proportional to $u^\#$, $u_0 = \exp(-j\pi u^\#)$. For this reconstruction we use the tenth iterations of the algorithm (36)–(40). The results obtained by the standard FFT and DDT algorithms are shown in Fig. 9. While numerically (RMSE = 0.186 for the DDT algorithm and RMSE = 0.26 for the FFT algorithm) the difference between the estimates is not large, the visual advantage of the DDT algorithm is quite obvious as it gives sharper and clearer imaging with no ringing effects along boundaries.

6. Object Wavefield Design

Assume that the object distribution u_0 should be selected in such a way that the wavefield distribution at a given distance $z = z^\#$ would be equal, or at least close to, a desired wavefield distribution $u_{z^\#}^\#$. It is not difficult to realize that formally this design problem is identical to the considered above reconstruction one. Indeed, let us replace the observed distribution

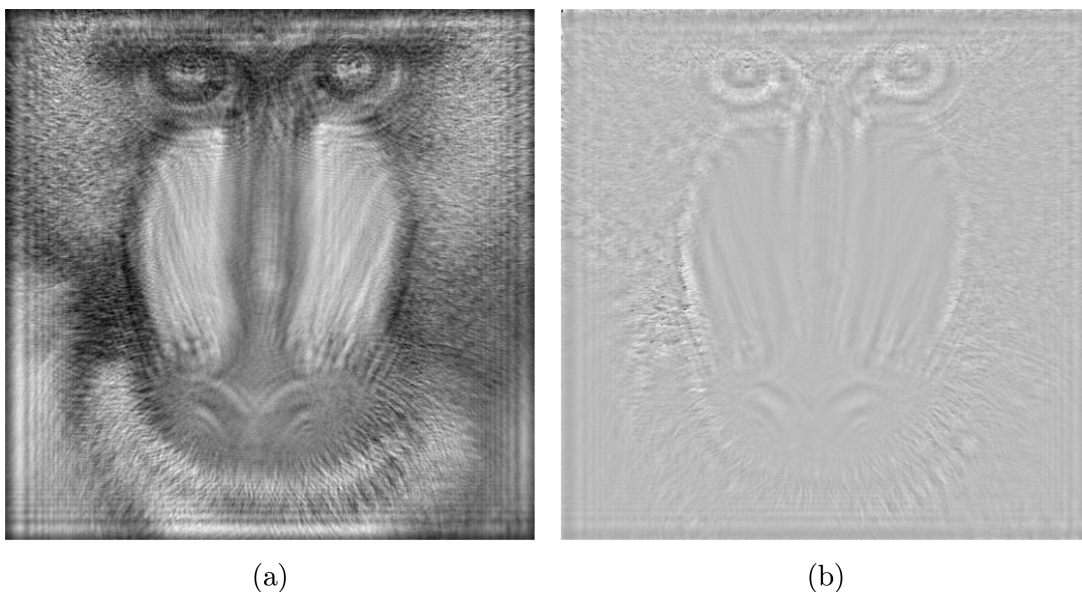


Fig. 6. Wavefield distribution at the sensor plane: (a) amplitude distribution; (b) phase distribution.

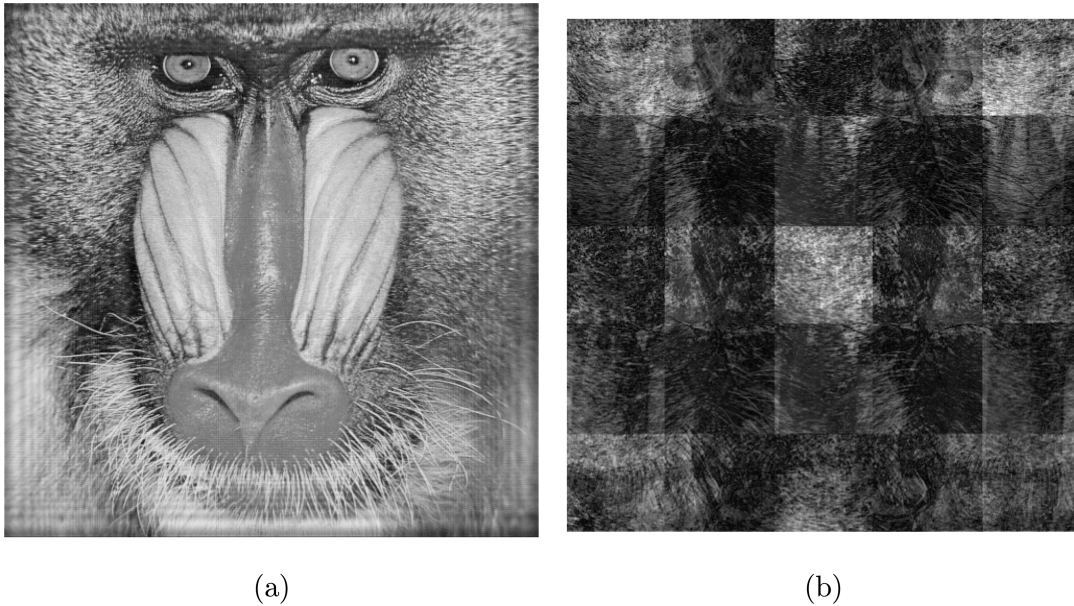


Fig. 7. Object wavefield reconstruction (amplitude distribution), double pixel size $\Delta = 3.9 \times 10^{-5}$: (a) inverse regularized DDT reconstruction, RMSE = 0.108; (b) standard FFT algorithm. The standard algorithm fails with a pattern of clear aliasing effects. DDT shows a good quality aliasing free reconstruction.

$u_z^\#$ by the corresponding desired one then the regularized inverse and the recursive regularized inverse algorithms give the unknown object distribution u_0 .

Let us exploit this approach for design of the object phase distribution such that the amplitude distribution at the sensor plane would have a desirable amplitude distribution. It is one of the typical settings for programming of the phase SLM used for generation of a given light intensity distribution.

For this problem we use the algorithm (36)–(40) where Eq. (37) is replaced by Eq. (42). In this way the algorithm varies only the phase of the object dis-

tribution trying to get the amplitude at the sensor plane close to $u_z^\#$ desired at the distance $z^\#$.

Figure 10 illustrates the obtained results. Figure 10(a) shows the obtained phase distribution for the object plane, while Fig. 10(b) demonstrates the quality of this design as it shows the predicted amplitude distribution at the sensor plane corresponding to the phase object with the phase distribution shown in Fig. 10(a). The curve in Fig. 11 demonstrates the convergence of the algorithm for this test. The results in Fig. 10 are achieved after 50 iterations of the algorithm. Numerically as well

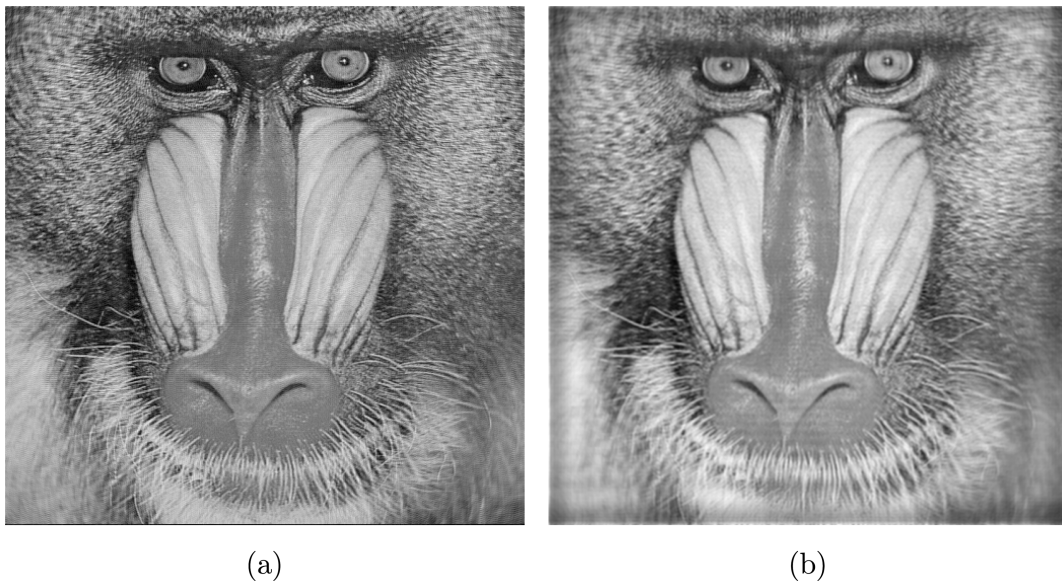


Fig. 8. Wavefield reconstruction (amplitude distribution): (a) the recursive regularized inverse DDT technique, RMSE = 0.051 after 10 iterations; (b) the standard FFT technique, RMSE = 0.086. The DDT algorithm shows sharper and better resolution imaging.

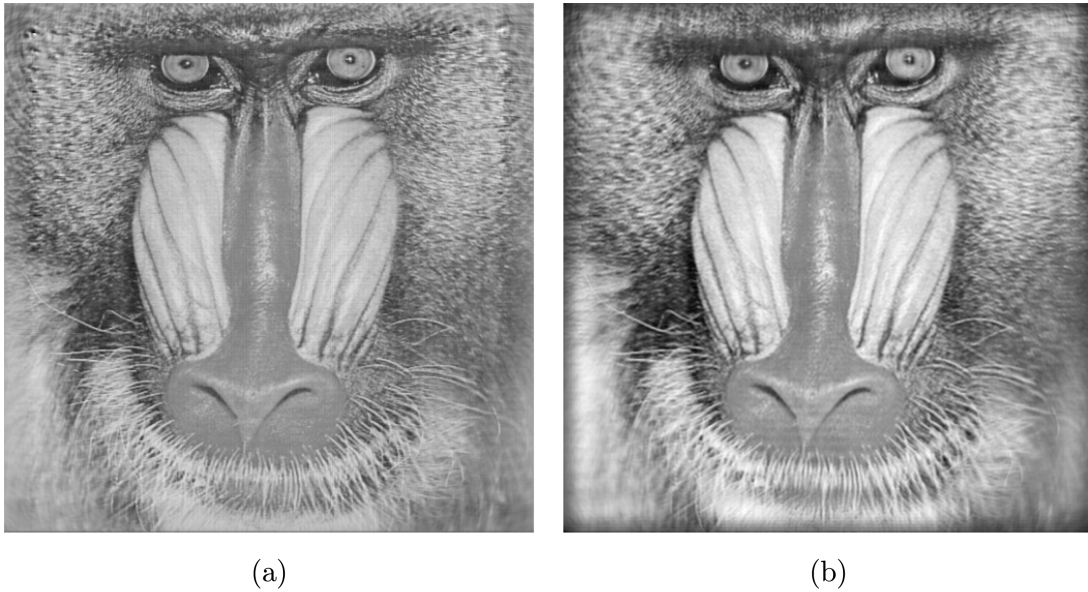


Fig. 9. Phase distribution reconstruction: (a) the recursive regularized inverse DDT technique, RMSE = 0.185 after 10 iterations; (b) the standard FFT technique, RMSE = 0.26. The DDT algorithm shows sharper and better imaging with no boundary ringing effect seen in the FFT reconstruction.

as visually [Fig. 10(b) versus Fig. 5) the results are quite good.

7. Conclusion

This paper concerns two aspects of discrete holography: discrete modeling of the forward wavefield propagation and inverse problems. The important property of the proposed DDT is that it accurately predicts the forward propagation for a pixelwise constant object distribution. This prediction is free of the aliasing effects typical for all standard discrete models.

The averaging of the observed intensities over the sensor pixel is not a new idea and is discussed in a number of publications (e.g., [1,2]). However, to the best of our knowledge, nobody has used it for aver-

aging both in the sensor and object domains, and, what is more important, to derive the operators corresponding to these averaged variables. The exact forward modeling makes this a reliable tool for evaluation of alternative algorithms by computer simulation.

The developed inverse technique is applied for two problems: distribution reconstruction in the object plane from observations given in the sensor plane and the design of the object plane distribution to obtain desired distribution in the sensor plane. Simulation experiments show a better accuracy and better imaging of the developed reconstruction techniques versus the standard FFT alternative.

The developed inverse algorithms similar to the standard FFT algorithm are not able to get a good

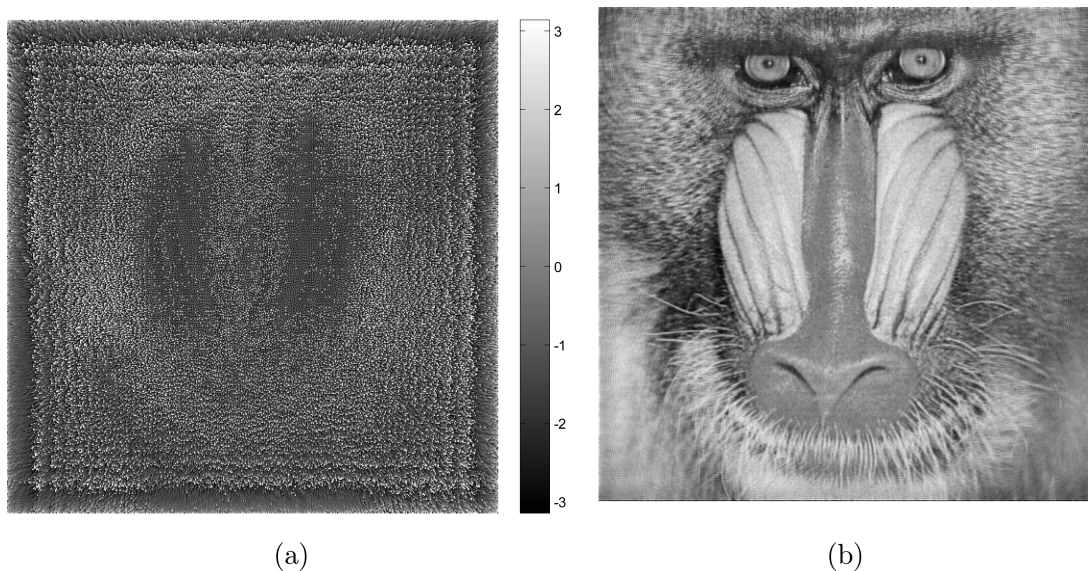


Fig. 10. Phase distribution design for the object plane to obtain a desirable amplitude distribution in the sensor plane: (a) designed phase distribution for the object plane; (b) the corresponding amplitude distribution in the sensor plane.

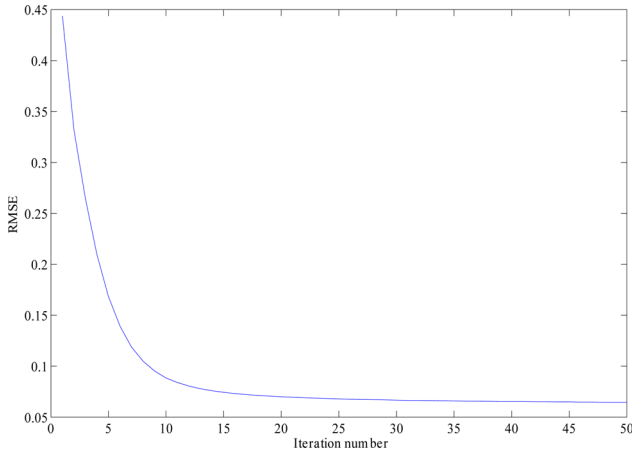


Fig. 11. (Color online) Convergence of the recursive regularized inverse phase design algorithm: RMSE versus the number of iterations.

quality reconstruction with sharp focussing for all values of the parameters Δ and z . However, numerically and visually, the DDT-based algorithm demonstrate a better performance.

One of the constructive ideas to improve the proposed frequency domain inverse algorithms is to use a sensor that is larger than that of the object aperture. The first promising results in this direction are reported in [15].

Finally, we note that DDT, as a discrete model for wavefield propagation, can be generalized to pixel sizes that are different in the object and sensor planes and applied to various optical settings used in digital holography.

We thank the anonymous referee for very fruitful and well-organized comments. We also thank Claass Falldorf from BIAS (Bremen, Germany) for comments and discussion. This work was supported by the Academy of Finland, project 213462 (Finnish Centre of Excellence program 2006–2011).

Appendix 1. Proof of Proposition 1.

Calculate $u_z[k, l]$ from Eqs. (19) and (20) using the inverse FFT:

$$u_z[k, l] = \frac{1}{N_a^2} \sum_{v_x, v_y = -N_a/2}^{N_a/2-1} W^{-v_x k} W^{-v_y l} \tilde{A}_z(v_x, v_y) \tilde{U}_0(v_x, v_y),$$

$$k, l = -N_z/2, \dots, N_z/2 - 1. \quad (\text{A1})$$

Inserting the expressions for $\tilde{A}_z(v_x, v_y)$ and $\tilde{U}_0(v_x, v_y)$ and changing the orders of summations we find

$$u_z[k, l] = \frac{1}{N_a^2} \sum_{u, v = -N_a/2+1}^{N_a/2-1} \sum_{u', v' = -N_0/2}^{N_0/2-1} a_z[u, v] u_0[u', v']$$

$$\times \sum_{v_y, v_x = -N_a/2}^{N_a/2-1} W^{-v_x(k-u-u')} W^{-v_y(l-v-v')}. \quad (\text{A2})$$

Noting that because of

$$\frac{1}{N_a^2} \sum_{v_y, v_x = -N_a/2}^{N_a/2-1} W^{-v_x(k-u-u')} W^{-v_y(l-v-v')}$$

$$= \delta(k-u-u') \delta(l-v-v'),$$

we obtain from Eq. (A2)

$$u_z[k, l] = \sum_{u, v = -N_a/2+1}^{N_a/2-1} \sum_{u', v' = -N_0/2}^{N_0/2-1} a_z[u, v] u_0[u', v']$$

$$\times \delta(k-u-u') \delta(l-v-v'). \quad (\text{A3})$$

This last formula gives the convolution (12) provided that for each k and $l = -N_z/2, \dots, N_z/2 - 1$ there are u and u' and v and v' , such that $u = k - u'$ and $v = l - v'$, provided that u and $v = -N_a/2 + 1, \dots, N_a/2 - 1$ and u' and $v' = -N_0/2, \dots, N_0/2 - 1$.

Let us test these requirements. We can see that

$$-N_z/2 - (N_0/2 - 1) \leq k - u' \leq N_z/2 - 1 + N_0/2,$$

i.e.,

$$-N_a/2 + 1 \leq k - u' \leq N_a/2 - 1.$$

It shows that for any $k = -N_z/2, \dots, N_z/2 - 1$ and any $u' = -N_0/2, \dots, N_0/2 - 1$, there always exist $u = k - u'$ such that $u = -N_a/2 + 1, \dots, N_a/2 - 1$.

In a similar way one can check that

$$-N_a/2 + 1 \leq l - v' \leq N_a/2 - 1,$$

there always exist $v = l - v'$ such that $v = -N_a/2 + 1, \dots, N_a/2 - 1$.

Then the formula (A3) can be rewritten in the form of Eq. (12),

$$u_z[k, l] = \sum_{u', v' = -N_0/2}^{N_0/2-1} a_z[k - u', l - v'] u_0[u', v'],$$

$$k, l = -N_z/2, \dots, N_z/2 - 1.$$

It proves that Eq. (20) gives a result identical to Eq. (12). Note that $N_a = N_0 + N_z$ is a minimal array size when these formulas are equivalent.

Appendix 2

Proof that

$$\frac{1}{\Delta} \int_{-\Delta/2}^{\Delta/2} \int_{-\Delta/2}^{\Delta/2} f(k\Delta + \xi' + \xi) d\xi d\xi'$$

$$= 2\Delta \int_{-1}^1 f(k\Delta + \Delta x) (1 - |x|) dx. \quad (\text{B1})$$

Consider the integral

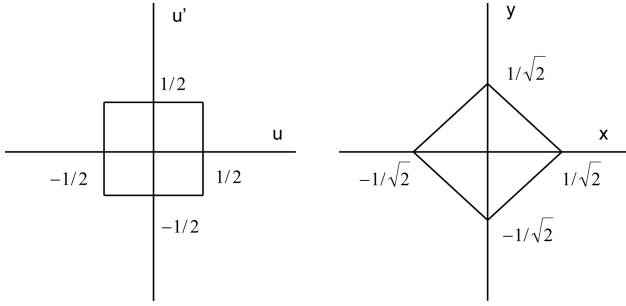


Fig. 12. Integration area in the original and transformed (rotated) coordinates.

$$\begin{aligned} J &= \frac{1}{\Delta} \int_{-\Delta/2}^{\Delta/2} \int_{-\Delta/2}^{\Delta/2} f(k\Delta + \xi' + \xi) d\xi d\xi' \\ &= \Delta \int_{-1/2}^{1/2} \int_{-1/2}^{1/2} f(k\Delta + \Delta u + \Delta u') du du', \end{aligned}$$

where f is a function of two variables and $u = \xi/\Delta$ and $u' = \xi'/\Delta$. Further, change the variables of integration according to the following formula

$$\begin{pmatrix} x \\ y \end{pmatrix} = \begin{pmatrix} \cos \varphi & \sin \varphi \\ -\sin \varphi & \cos \varphi \end{pmatrix} \begin{pmatrix} u \\ u' \end{pmatrix}. \quad (\text{B2})$$

With $\varphi = \pi/4$ this orthogonal transformation means a rotation of the integration area on the angle $\pi/4$ as shown in Fig. 12.

For $\varphi = \pi/4$ the new variables are defined as

$$\begin{pmatrix} x \\ y \end{pmatrix} = \frac{1}{\sqrt{2}} \begin{pmatrix} 1 & 1 \\ -1 & 1 \end{pmatrix} \begin{pmatrix} u \\ u' \end{pmatrix}, \quad (\text{B3})$$

and according to Fig. 12 the following sequence of transformations can be done:

$$\begin{aligned} J &= \Delta \int_{-1/2}^{1/2} \int_{-1/2}^{1/2} f(k\Delta + \Delta u + \Delta u') du du' \\ &= \Delta \int_0^{1/\sqrt{2}} f(k\Delta + \Delta\sqrt{2}x) \int_{-1/\sqrt{2}+x}^{1/\sqrt{2}-x} dy dx \\ &\quad + \Delta \int_{-1/\sqrt{2}}^0 f(k\Delta + \Delta\sqrt{2}x) \int_{-1/\sqrt{2}-x}^{1/\sqrt{2}+x} dy dx \\ &= \Delta \int_0^{1/\sqrt{2}} f(k\Delta + \Delta\sqrt{2}x) 2(1/\sqrt{2} - x) dx \\ &\quad + \Delta \int_{-1/\sqrt{2}}^0 f(k\Delta + \Delta\sqrt{2}x) 2(1/\sqrt{2} + x) dx \\ &= 2\Delta \int_{-1/\sqrt{2}}^{1/\sqrt{2}} f(k\Delta + \Delta\sqrt{2}x) 2(1/\sqrt{2} - |x|) dx \\ &= 2\Delta \int_{-1}^1 f(k\Delta + \Delta x') (1 - |x'|) dx'. \end{aligned}$$

The last expression proves (B1).

Appendix 3. Proof of Proposition 3.

If the conditions (28) hold there is a one-to-one link between the extended object and sensor wavefield distributions. In the frequency domain this link means that

$$\begin{aligned} \tilde{U}_z(v_x, v_y) &= \tilde{A}_z(v_x, v_y) \tilde{U}_0(v_x, v_y), \\ \tilde{U}_0(v_x, v_y) &= \tilde{A}_z^{-1}(v_x, v_y) \tilde{U}_z(v_x, v_y), \\ k, l &= -N_a/2, \dots, N_a/2 - 1. \end{aligned} \quad (\text{C1})$$

For the spatial domain representation in the form (29) it means that the matrix \mathcal{A}_z is nonsingular.

References

1. Th. Kreis, *Handbook of Holographic Interferometry (Optical and Digital Methods)* (Wiley-VCH, 2005).
2. I. Yamaguchi, J. Kato, S. Ohta, and J. Mizuno, "Image formation in phase-shifting digital holography and applications to microscopy," *Appl. Opt.* **40**, 6177–6186 (2001).
3. V. Katkovnik, J. Astola, and K. Egiazarian, "Wavefield reconstruction and design as discrete inverse problems," *Proceedings of 3D TV Conference, Istanbul* (2008).
4. G. S. Sherman, "Integral-transform formulation of diffraction theory," *J. Opt. Soc. Am.* **57**, 1490–1498 (1967).
5. J. W. Goodman, *Introduction to Fourier Optics* (McGraw-Hill, 1996) 2nd edition.
6. L. Onural, "Exact analysis of the effects of sampling of the scalar diffraction field," *J. Opt. Soc. Am. A* **24**, 359–367 (2007).
7. F. Shen and A. Wang, "Fast-Fourier-transform based numerical integration method for the Rayleigh–Sommerfeld diffraction formula," *Appl. Opt.* **45**, 1102–1110 (2006).
8. J. M. Arnold, "Phase-space localization and discrete representations of wave fields," *J. Opt. Soc. Am. A* **12**, 111–123 (1995).
9. L. Onural, "Some mathematical properties of the uniformly sampled quadratic phase function and associated issues in digital Fresnel diffraction simulations," *Opt. Eng.* **43**, 2557–2563 (2004).
10. I. Aizenberg and J. Astola, "Discrete generalized Fresnel functions and transforms in an arbitrary discrete basis," *IEEE Trans. Signal Process.* **54**, 4261–4270 (2006).
11. M. Liebling, Th. Blu, and M. Unser, "Fresnelets: new multiresolution wavelet bases for digital holography," *IEEE Trans. Image Process.* **12**, 29–43 (2003).
12. M. Bertero and P. Boccacci, *Introduction to Inverse Problems in Imaging* (IOP Publishing, 1998).
13. A. N. Tikhonov and V. Y. Arsenin, *Solution of Ill-Posed Problems* (Wiley, 1977).
14. V. Katkovnik, K. Egiazarian, J. Astola, *Local Approximation Techniques in Signal and Image Processing* (SPIE, 2006).
15. V. Katkovnik, J. Astola, and K. Egiazarian, "Numerical wavefield reconstruction in phase-shifting holography as inverse discrete problem," submitted to EUSIPCO 2008 (2008).